

# Integration of Physics Based Weight Models into Rotorcraft Design Sizing

Bharath Govindarajan<sup>1</sup>, Ananth Sridharan<sup>1</sup>, and Michael Avera<sup>2</sup>

<sup>1</sup>Assistant Research Scientist, Department of Aerospace Engineering, College Park, MD, USA

<sup>2</sup>Aerospace Engineer, U.S. Army Research Laboratory, Aberdeen, MD, USA

## ABSTRACT

The availability of an accurate empty weight model for each rotorcraft component is critical for synthesizing efficient vehicles, because over-designing one component in a flying platform results in a higher take-off weights, more installed power and smaller reduced useful load fraction. Traditionally, these models are synthesized using statistical data, which are unavailable for unconventional, medium-scale and next-generation VTOL configurations. This paper presents a methodology for design sizing of unconventional rotorcraft using physics-based weight models for the primary load-carrying members. This methodology is demonstrated for a quad-rotor bi-plane tailsitter hybrid configuration, which can operate in both fixed-wing and airplane mode. A beam lattice framework for the airframe structure, and the spar geometry in the rotor blade are iteratively adjusted during design sizing to accommodate the expected wing loads and rotor blade loads. Using this analysis, a consistent combination of vehicle macro-dimensions (rotor radius, tip speed, wing span) as well as detailed design parameters (spar height, skin thickness and cross-section weight) are obtained simultaneously.

## INTRODUCTION AND MOTIVATION

Rotorcraft preliminary design and sizing of full-scale configurations is typically performed with statistical data and reduced-order models for empty weight and performance. These models were constructed several decades earlier, when computational power was restricted and higher-fidelity models were unavailable or impractical to use during initial sizing. However, present levels of computing power are several orders of magnitude greater compared to when these reduced-order models were conceptualized. These reduced-order models are also based on certain assumptions that may not be applicable to next-generation rotorcraft, such as the construction materials. Therefore, it is advantageous to systematically replace each of the reduced-order models with higher-fidelity counterparts, to expand the applicability of the sizing analysis. The particular focus of this paper is to obtain physics-based weight models for select helicopter components, and compare the predictions of vehicle weight and size obtained using the high-fidelity model with the corresponding legacy counterparts for various rotorcraft scales.

Next-generation rotorcraft include innovative design concepts for full-scale and a plethora of VTOL concepts investigated by various organizations for small-scale unmanned air vehicles, drones and personal transport. The state-of-the-art in rotorcraft sizing was introduced by NDARC, NASA's code for Design and Analysis of Rotorcraft Configurations (Ref. 1). This framework has been used to successfully size various full

scale configurations, such as single main rotor, coaxial, tandem rotors and tilt-rotors. However, such NDARC-type formulations rely on weight models that are based on full-scale production designs. Owing to this dependency, ad-hoc modifications may be necessary to extend the approach for sizing small-scale VTOL concepts.

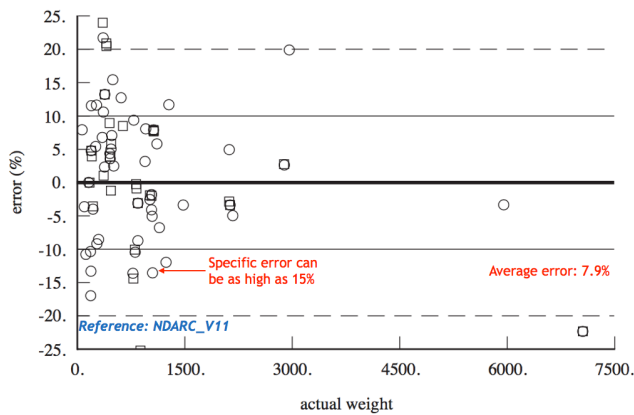
Another limitation of this approach is the relatively lower fidelity models used for performance (to estimate power required) within the sizing loop, because of the computational cost associated with higher fidelity tools. However, performance maps from comprehensive analysis (performed prior to sizing) have been used in conjunction with NDARC (Ref. 2) for a range of parametric conditions such as vehicle GTOW, advance ratio and high-lift device setting. While this strategy includes higher-fidelity performance models indirectly, these maps must be regenerated for different flight conditions and rotor configurations — a computationally expensive undertaking and one that requires extensive ad hoc tuning.

Recently, Sridharan et al. (Ref. 3) used a design framework with comprehensive analysis-based performance for vehicle sizing, where the intention was to obtain power predictions from higher-fidelity models such as a free-vortex method within the sizing loop. The computational cost was mitigated through the use of Graphics Processing Units (GPUs) to parallelize the code. A three-stage process was used to systematically incorporate aspects of blade aerodynamic design into preliminary sizing. The first stage used simplified performance models to eliminate clearly infeasible combinations of design parameters, and these results were used as an initial guess for the second stage. Vehicle sizing with the compre-

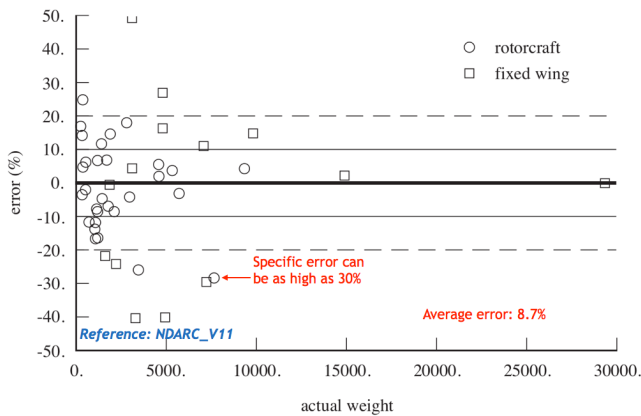
| Group Name               | Description | Dominant Dependencies                                 |
|--------------------------|-------------|---|
| Fixed wing               | AFDD93      | <b>Weight</b> , wing aspect ratio                     |
| Rotor                    | AFDD00      | <b>Radius, solidity</b> , flap frequency              |
| Empennage                | Custom      | <b>Radius</b>   |
| Propeller                | AFDD82      | Vehicle drag → <b>Weight</b>                          |
| Fuselage                 | AFDD82      | <b>Weight, radius</b>                                 |
| Alighting gear           | AFDD82      | <b>Weight</b>   |
| Engine                   | Custom      | Max. Power → Drag → <b>Weight</b>                     |
| Air Induction            | AFDD82      | Engine weight → Max. Power → D → <b>Weight</b>        |
| Fuel system              | AFDD82      | Fuel flow rate per engine → Power → D → <b>Weight</b> |
| Drive system             | AFDD00      | Max torque → RPM, Power → D → <b>Weight</b>           |
| Flt. Control, Hydraulics | AFDD82      | $N_b$ , $N_R$ , <b>solidity, radius</b> , $V_{TIP}$   |
| Deicing                  | AFDD        | $N_R$ , <b>radius, solidity</b>                       |

Radius and solidity drive the rotor system weight, which permeates through to the other weight groups

Fig. 1. Dominant dependencies of the AFDD empty weight models



(a) Blade weight



(b) Fuselage weight

Fig. 2. Data scatter in: (a) Rotor blade weight model, and (b) Airframe weight model (Ref. 1).

hensive analysis-based performance estimates was performed in the second stage, and the “best” configuration was chosen. Finally, the blade geometry was further refined to reduce rotor power requirements in high-speed cruise.

Figure 1 shows the dominant dependencies of the empty groups in the AFDD model. The first column is the group name, the second is the designation of the AFDD model, and the third column shows the driving dependencies that affect the weight of the component. The empty weight of each helicopter component is driven by the gross take-off weight, rotor radius and rotor solidity. Ignoring the cyclic dependency of empty weight on GTOW, it is evident that the empty weight (and therefore, total vehicle weight) is driven primarily by rotor radius and solidity. According to the nature of the empty weight models, The rotor group weight drives the sizing of other components. Therefore, it is crucial to use accurate weight models for the rotor blade and hub, because errors in this critical component cascades into corresponding errors in all other components of the rotorcraft.

Though the role played by the rotor blade empty weight model in sizing is crucial, it is still based on statistical data and has almost 8% mean fit error. Figure 2(a) shows the weight of the rotor blade against the gross-takeoff weight (GTOW) of 51 full-scale vehicles, which represents the data used by the AFDD00 empty weight model (Ref 1). Significant scatter in the data is observed, especially at lower weight classes, i.e., below 1,500 lb GTOW. The empirical fit results in an average error of 7.9% with specific errors as high as 15%. These errors in the empty weight model propagate into the overall sizing and result in over-designed (or worse, under-designed) components. A similar trend is observed in Fig. 2(b), which shows an average error of 8.7% in the prediction of fuselage weight with a specific error as high as 30%. While Fig. 2

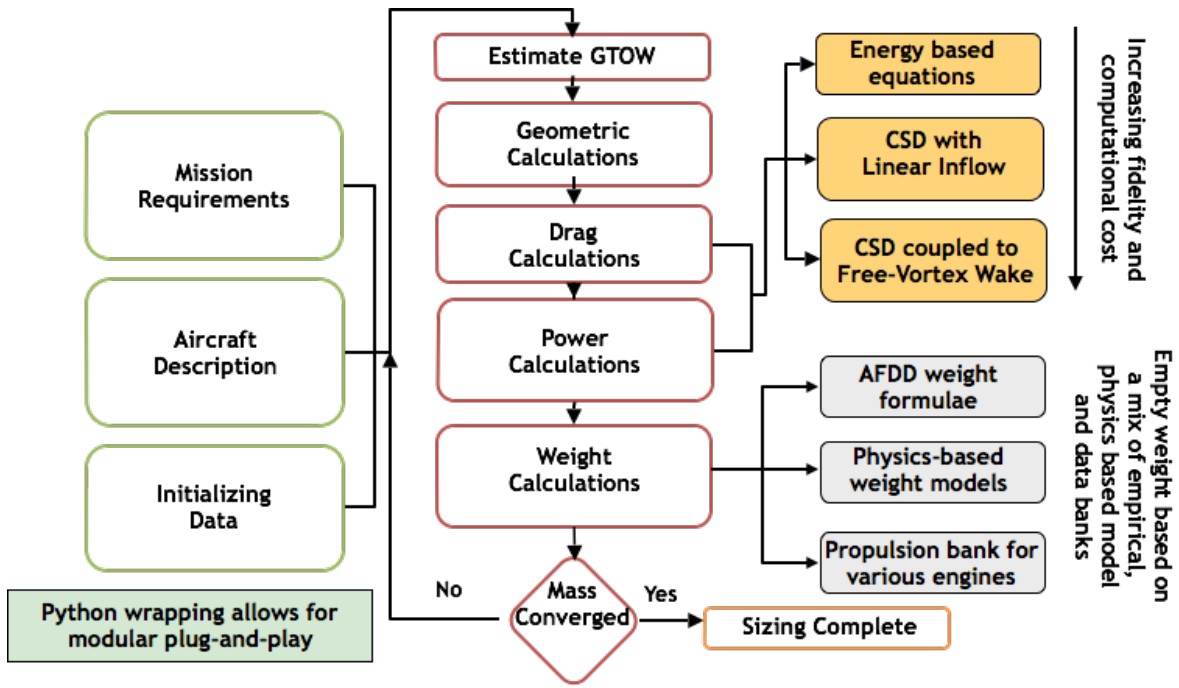


Fig. 3. Schematic of the sizing framework with the integration of comprehensive analysis and physics based empty weight models.

relates to blade weight and airframe weight, these trends are typical of most empty weight components, which highlight the challenge in generating reliable empty weights for a given configuration.

To refine the design of the entire vehicle, it is critical to ensure accurate weight estimates for the various sub-groups. The objective of this work, and its improvements over preceding analyses is the inclusion of physics-based models for rotor blade weight and the airframe based on the stresses and loads experienced by the respective structures. Such an approach has been presented by NASA for fixed-wing aircraft (Ref. 4) for sizing the load-carrying members in the fuselage and wings of a transport airplane; this approach is adapted for use in a modern VTOL platform.

## METHODOLOGY

### HYDRA: Overview

The HYbrid Design and Rotorcraft Analysis (HYDRA) framework (Ref. 3) is an integrated analysis and design tool used to perform conceptual rotorcraft design for arbitrary user-selected rotorcraft configurations. These configurations include a conventional helicopter, coaxial compound with lift and thrust augmentation, tilt-rotor, and asymmetric single rotor compounds. Although initially implemented with low-fidelity performance models typical of conceptual design tools, the architecture allows for multi-fidelity design optimization.

### Preliminary Design and Iterative Sizing

The iterative sizing method in HYDRA is based on Tishchenko's original helicopter design methodology (Ref. 5), and is used to size a vehicle for a target mission and specified payload. The sizing analysis provides estimates of the vehicle take-off weight, rotor dimensions, installed power and fuel required for a user-specified aircraft description. The description of the aircraft includes the number of engines and lifting/thrusting components (rotors, wings and propellers), their relative placement and orientation with respect to the airframe. The mission profile consists of a combination of idle, hover, climb/descent and cruise phases and the corresponding atmospheric conditions for each phase, i.e., density altitude and temperature. The sizing methodology has been validated against the NASA Design and Analysis of Rotorcraft Code (NDARC) for various mission profiles, and also against various production rotorcraft (Ref. 3). A schematic of the sizing analysis and its various components is shown in Fig. 3. AFDD empty weight models for various components as given in NDARC (Ref 1) are used to size non-structural weight groups as well as structural weight groups for conventional helicopters and tilt-rotors.

### Performance Model

A key feature of the HYDRA framework is that it allows for direct integration of a high-fidelity performance analysis (including the elastic blade dynamics) for power calculations during sizing (Ref. 6). In HYDRA, a rotorcraft comprehensive analysis (Ref 7) with an integrated free wake analysis

(Ref 8) is used to provide accurate estimates of loads, vibration and performance over all flight conditions. The inclusion of higher-order models is critical for accurate performance predictions at advance ratios of 0.5 and above, where low-fidelity models have to be tuned on a case-by-case basis (again, using a high-fidelity model) to maintain accuracy. This approach is similar to that presented by Moodie and Yeo (Ref. 9), with one main distinction – instead of repeatedly calibrating a lower-fidelity performance model, rotor power is directly calculated using a high-fidelity analysis during sizing iterations.

## Propulsion Model

A scalable turboshaft engine was used in the present work. The turboshaft engine burns fuel, and the corresponding weight reduction over the course of the mission is modeled as discrete jumps across mission segments. The corresponding specific fuel consumption (SFC) variation with power is given by

$$\text{SFC} = 1.24 \exp(-0.05671P) + 0.3329 \exp(-0.0002414P) \quad (1)$$

where  $P$  is the required power in hp and SFC is given in lb/hp-hr. Engine weight is scaled linearly with the power required using the UH-60A as a reference, i.e.,

$$\text{Engine Weight} = \frac{450 \text{ lb}}{1,620 \text{ SHP}} \times \text{Installed Power, HP.} \quad (2)$$

## Physics Based Model for Rotor Blades

One of the most significant drivers of vehicle weight is the rotor group weight. Like other empty weight components, it is driven by a combination of vehicle dimensions and user-prescribed parameters. One such empirical parameter is the flap natural frequency. In the legacy approach for estimating rotor blade weight, the designer had to prescribe this parameter to perform sizing. However, underlying data for the flap frequency does not extend beyond 1.08/rev, i.e. for articulated and hingeless rotors with flexures. For small-scale VTOL with very stiff rotor systems ( $v_\beta \geq 1.4/\text{rev}$ ), extrapolation of the trend line beyond the range of available data for  $v_\beta$  may yield erroneous estimates for rotor blade weight. An alternate approach is presented in this section, where a physics-based model is used to obtain blade weight estimates.

A schematic of the blade spar and cross-section parameters is shown in Fig. 4. The cross-section of the airfoil consists of a trapezoidal spar, skin, honeycomb material and a leading edge weight. For each of these four components, materials are assigned from a database consisting of mass density, Young's modulus and allowable stress/strain in compression and tension. The cross-section geometry is parameterized by; (a) spar wall thickness, (b) skin thickness, (c) spar web locations  $X_{s1}$ ,  $X_{s2}$  and (d) spar web heights  $2h_{s1}$ ,  $2h_{s2}$ . A leading edge weight, if required, is placed so that the effective center of mass lies at or ahead of the quarter chord location.

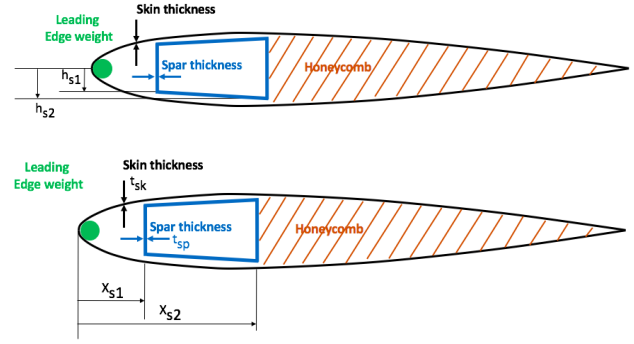


**Fig. 4. Design variables for rotor airfoil sections**

In this work, the load-bearing components of the airfoil section are designed so that the neutral axis and CG both lie at quarter-chord. A NACA-0012 section is used to estimate cross-section areas, moments of inertia and moments of area for the filler material (rohacell), skin (+/- 45 deg carbon fiber sheet) and spar (Titanium, Aluminum, 0/90 carbon fiber or uniaxial carbon fiber). In this case, the load-bearing elements are the carbon fiber skin and Titanium spar.

Consider first the skin of the rotor blade. If a uniform skin thickness is assumed along the contour of the airfoil, then the neutral axis is aft of the 40% chord location. Alternately, if 9 layers of skin are used from  $x/c = 0$  to  $x/c=0.25$ , and one layer of skin from  $x/c=0.25$  to  $x/c = 1.0$  on both upper and lower surfaces, the neutral axis and center of mass of the spar both lie just ahead of quarter-chord, a structurally and aerodynamically significant location for rotor blades. This design is shown schematically in Fig. 5. For full-scale vehicles, this construction is useful, because the size of the smallest machinable layer is a small fraction of the available thickness. (For small-scale vehicles, the skin thickness is held uniform around the contour and the spar is repositioned inside the blade to shift the neutral axis back to quarter-chord). If required, leading edge weights are also used to place the section center of gravity (CG) at quarter chord.

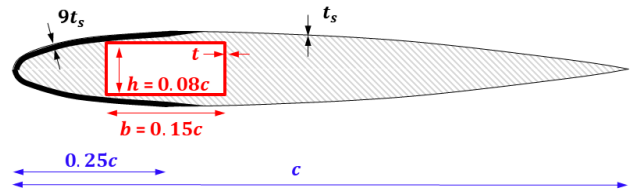


**Fig. 5. Airfoil section for rotor blades: layout of load-carrying members**

The first and second area moments of inertia for the skin and spar are computed for a NACA 0012 section numerically. For the 9:1 layer ratio, the constants are:

1. Skin second moment of area, lag axis  $I_{zz_s} = 0.39301c^3t_s$
2. Skin second moment of area, flap axis  $I_{yy_s} = 0.01367c^3t_s$

3. Skin area  $A_s = 6.41767ct_s$
4. Filler area  $A_f = 0.082179c^2$
5. Filler first moment of area  $\int x dA_f = 0.03456c^3$
6. Skin first moment of area  $\int x dA_s = 1.53868c^2t_s$
7. Contour integral  $\oint \frac{ds}{t_s} = 1.55266c/t_s$
8. Filler second moment of area  $\int ((x - 0.25)^2 + y^2) dA_f = 0.006993c^2$

The terms  $c$  and  $t_s$  refer to the airfoil chord and skin thickness from  $x = 0.25c$  to  $x = c$ . The coordinates  $x$  and  $y$  are normalized with respect to the airfoil chord, and measured with respect to an origin at the leading edge centerline.

The second load-carrying member in the cross-section is the spar. The spar is assumed to be a hollow rectangle with 2 webs and 2 flanges of equal thickness  $t$ . The width of the box beam is  $b$  and the height is  $h$ . The center of the spar is placed at quarter-chord (for full-scale vehicles), so that the neutral axis and section center of gravity are both just ahead of  $x=0.25c$ . For sub-scale vehicles, the spar is placed in the cross-section so as to shift the neutral axis back to quarter-chord. The spar height is set to  $h=0.08c$  (full scale) or  $h=0.1c$  (sub-scale), and the spar width is set to  $b=0.15c$ . The only free variables that can be used as design parameters are the spar thickness  $t$  and the skin thickness  $t_s$ .

With rotor radius  $R$ , rotor speed  $\Omega$  and peak torque at the blade root  $Q_b$  obtained from sizing, the vertical force on the blade is obtained by dividing the maximum expected thrust level by the total number of blades as

$$F_z = \frac{W}{N_R N_b} n_z \quad (3)$$

The terms  $n_z$  is a load factor that can incorporate additional margins of safety for blade loads. The flap bending moment at the root is computed assuming the entire blade vertical force is applied as a concentrated load at 75% span, and the lag bending moment at the root is equal to the blade torque. Therefore,

$$M_z = F_z(0.75R) \quad (4)$$

$$M_y = Q_b n_z \quad (5)$$

For full-scale vehicles, all loads are carried in the spar. However, the skin provides comparable flap bending stiffness for sub-scale vehicles, and its contribution to bending stiffness cannot be ignored. The flap bending moments in the spar and skin are proportional to their relative contributions to flap bending stiffness, i.e.

$$M_{y\text{spar}} = M_y \frac{EI_{yy\text{spar}}}{EI_{yy\text{total}}} \quad (6)$$

$$M_{y\text{skin}} = M_y \frac{EI_{yy\text{skin}}}{EI_{yy\text{total}}} \quad (7)$$

Similar expressions are used to find the lag bending moments in the spar and skin. The tensile bending stress due to vertical loads at the root is given by

$$\sigma_{xx,1\text{spar}} = \frac{M_{y\text{spar}} 0.5h}{I_{yy\text{spar}}} \quad (8)$$

$$\sigma_{xx,1\text{skin}} = \frac{M_{y\text{skin}} 0.05c}{I_{yy\text{skin}}} \quad (9)$$

The tensile stresses due to blade torque at the root is

$$\sigma_{xx,2\text{spar}} = \frac{M_{z\text{spar}} 0.5b}{I_{yy\text{spar}}} \quad (10)$$

$$\sigma_{xx,2\text{skin}} = \frac{M_{z\text{skin}} 0.25c}{I_{yy\text{skin}}} \quad (11)$$

Assuming a uniform cross-section for the entire blade, the total mass per unit span of the cross-section  $m$  (sum of spar, skin and filler material) is used to compute the centrifugal force at the root  $T$  as

$$T = 0.5m\Omega^2 R^2 \quad (12)$$

The axial stresses in the spar and skin due to centrifugal force are obtained using the ratios of their axial stiffnesses as

$$\sigma_{xx,3\text{spar}} = \frac{T}{A_{\text{spar}}} \frac{EA_{\text{spar}}}{EA_{\text{total}}} = \frac{T_{\text{spar}}}{A_{\text{spar}}} \quad (13)$$

$$\sigma_{xx,3\text{skin}} = \frac{T}{A_{\text{skin}}} \frac{EA_{\text{skin}}}{EA_{\text{total}}} = \frac{T_{\text{skin}}}{A_{\text{skin}}} \quad (14)$$

$$(15)$$

The total axial stiffness of the cross-section is given by the sum of the individual contributions from the spar and skin, i.e.

$$EA_{\text{total}} = EA_{\text{spar}} + EA_{\text{skin}}$$

The axial stresses due to centrifugal force are tensile and equal at all points along the cross-section. However, the axial stresses due to lag bending and flap bending are either tensile or compressive depending on the location of the point in the cross-section. For the skin, lag bending causes tensile stress at the leading edge, while flap bending causes tensile stress at the bottom surface. The corner at the intersection of the bottom flange and web near the leading edge experiences maximum tensile stress in the spar. Therefore, the peak axial stresses in the skin and spar are obtained from superposition as

$$\sigma_{xx\text{spar}} = \sigma_{xx,1\text{spar}} + \sigma_{xx,2\text{spar}} + \sigma_{xx,3\text{spar}} \quad (16)$$

$$\sigma_{xx,LE\text{skin}} = \sigma_{xx,1\text{skin}} + \sigma_{xx,3\text{skin}} \quad (17)$$

$$\sigma_{xx,BS\text{skin}} = \sigma_{xx,2\text{skin}} + \sigma_{xx,3\text{skin}} \quad (18)$$

The subscripts *LE* and *BS* refer to the leading edge and bottom surface for the skin. As a worst-case estimate, the maximum possible tensile stress in the skin is limited to

$$\sigma_{xx\text{skin}} \leq \sigma_{xx,1\text{skin}} + \sigma_{xx,2\text{skin}} + \sigma_{xx,3\text{skin}} \quad (19)$$

Recall that the only free variables in this design are the thickness of the skin  $t_s$  and the thickness of the spar  $t$ . First, we modify the spar thickness to limit the peak tensile stress to the maximum allowed value for the material. The expression for peak tensile stress in the spar may be expanded analytically as

$$\sigma_{xx\text{spar}} = \frac{T_{\text{spar}}}{2(b+h)t} + \frac{M_{y\text{spar}}0.5h}{0.5bt^2 + \frac{1}{6}th^3} + \frac{M_{z\text{spar}}0.5b}{0.5ht^2 + \frac{1}{6}tb^3} \quad (20)$$

The stress levels are inversely proportional to the chosen design parameter  $t$ , i.e. the spar thickness. Based on an initial guess, the tensile stress is predicted and the spar thickness is adjusted so that the maximum tensile stress  $\sigma_{xx\text{spar}}$  does not exceed the allowed stress for the spar material  $\sigma_{\text{yield}}$ . This criterion leads to the following fixed-point update expression for the spar thickness as

$$t^{n+1} = 1.05 \frac{\sigma_{xx\text{spar}}(t=t^n)}{\sigma_{\text{yield}}} t^n \quad (21)$$

The factor 1.05 provides an additional 5% margin between the limit load stress and failure.

The skin thickness is adjusted based on two criteria. The first criterion is that the maximum tensile stress does not exceed the yield strength for the material. It was observed that after the spar thickness  $t$  converged, the maximum tensile stress in the skin  $\sigma_{xx\text{skin}}$  is well within the allowable limit. Therefore, another criterion is chosen to set the skin thickness: the first natural torsion frequency of the rotor blade must be 4.4/rev, i.e. sufficiently high so as to not exhibit significant elastic twist. The skin thickness is adjusted using the following analytical calculations.

The polar mass moment of inertia for the cross-section  $I_\theta$  is computed numerically based on the mass density and polar moments of area  $I_{xx}$  for the spar, skin and filler material, using current values of rotor blade chord (obtained from rotor solidity, disk loading and gross take-off weight). The first rotating blade torsion frequency is given by

$$\omega_\theta = \sqrt{\omega_{\theta_0}^2 + \Omega^2} \quad (22)$$

The first non-rotating blade torsion frequency is given by

$$\omega_{\theta_0} = \frac{\pi}{2} \sqrt{\frac{GJ}{I_\theta R^2}} \quad (23)$$

The primary role of the skin is to provide torsional stiffness. The effective torsional stiffness of a closed cross-section is given by

$$GJ = \frac{4GA^2}{\oint \frac{ds}{t_s}} \quad (24)$$

$GJ$  is the torsional stiffness,  $G$  is the shear modulus,  $A$  is the area in the closed loop (cross-sectional area),  $s$  is the coordinate along the perimeter of the section and  $t_s$  is the local skin thickness. For the 9:1 skin thickness ratio that places the CG

and neutral axis at the quarter-chord, the integral evaluates to  $1.553 \frac{c}{t_s}$ , where  $t_s$  is the skin thickness at the trailing edge.

Rearranging these expressions, the thickness of the single-layer skin  $t_s$  can be obtained as

$$t_s^{n+1} = 2.889 \frac{cI_\theta(\Omega R)^2}{GA^2} (t_s = t_s^n) \quad (25)$$

For carbon fiber, the minimum thickness of a single ply is 0.5mm. Therefore, if  $t_s$  is less than 0.5 mm, then it is rounded up to 0.5 mm. The fixed-point iteration update for skin thickness is performed together with the update for the spar thickness. For the nature of the mission investigated, the skin thickness is always driven by manufacturing limits ( $t_s = 0.5$  mm) rather than torsion frequency. The fixed-point iterations are terminated when spar thickness changes by less than 0.1% across iterations. For this update scheme, a non-zero initial guess is required for  $t$ , but not  $t_s$ .

Further, by placing the CG and neutral axis near the quarter-chord, the penalty for adding balancing weights is mitigated, resulting in reduced empty weight.

### Physics Based Model for Airframe Sizing

The AFDD82 fuselage model for helicopter is given by

$$w_{\text{fuselage}} = w_{\text{basic}} + w_{\text{press}} + w_{\text{cw}} \quad (26)$$

where  $w_{\text{basic}}$  is the basic weight of the fuselage,  $w_{\text{press}}$  is the weight from any pressurization constraints (set to none for the sample mission in this work) and  $w_{\text{cw}}$  is the weight addition for crashworthiness, which is assumed to be 6% of the basic weight as per AFDD standards. The basic weight is given by

$$w_{\text{basic}} = 5.896 f_{\text{ramp}} \left( \frac{W_{\text{GTOW}}}{1000} \right)^{0.4908} n_z^{0.1323} S_{\text{body}}^{0.2544} l^{0.61} \quad (27)$$

where  $f_{\text{ramp}}$  is the factor for a retractable ramp,  $n_z$  is the load factor,  $S_{\text{body}}$  is the wetted area of the fuselage and  $l$  is the length of the fuselage. While these terms can be defined for full-scale helicopters/tiltrotor, their definitions become increasingly challenging to interpret in the context of unconventional configurations such as a quad-rotor. Additionally, even if such a definition can be codified, the accuracy of the model at small take-off weights (less than one ton) is questionable – see Fig. 2(b).

In the present work, the airframe is defined as a beam lattice framework and the loads on the structure are computed using a finite element analysis (FEA). The external loads on the structure arise from the weight of different components and the dominant aerodynamics loads (rotor thrust and wing lift). A set of three-dimensional Euler-Bernoulli beam elements with six degrees of freedom at each node (three translations and three rotations) was assembled in a finite element framework. After discretization of the distributed loads into equivalent concentrated forces, the static deflection is obtained and used to compute bending stresses. By requiring

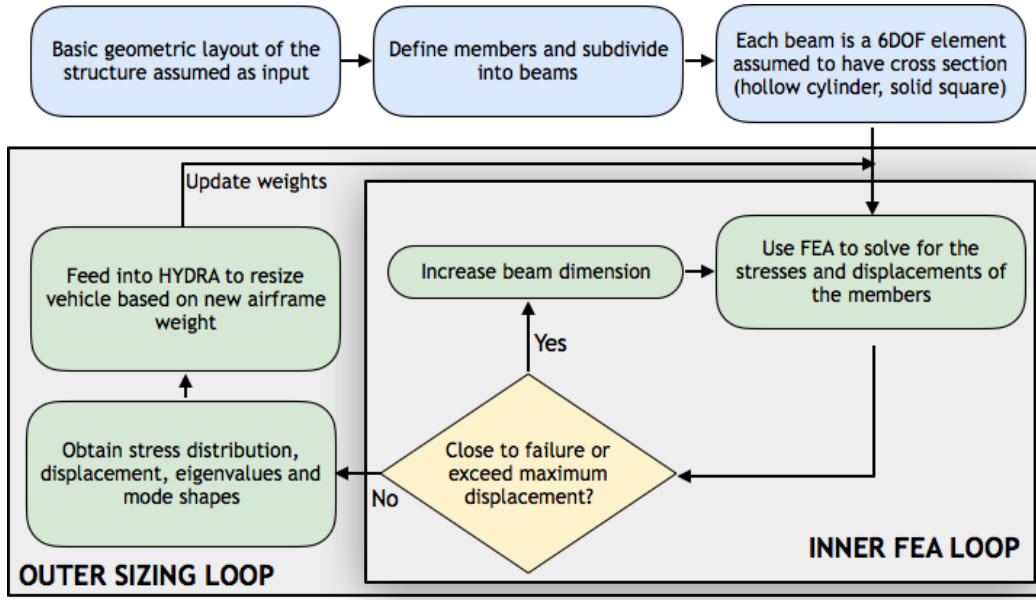


Fig. 6. Flowchart depicting the inclusion of the finite element analysis within the sizing framework.

each element in the structure to operate within a band of a target safety factor, and not exceed a maximum absolute limit for bending deflection, beam cross-section dimensions are iteratively adjusted in an inner loop within the sizing framework. The overall process is depicted in a flowchart shown in Fig. 6 and proceeds as follows

1. **Initialize:** A geometric layout of the airframe is chosen, and beam elements are defined. The present work assumes the beam cross section to be simple shapes such as a hollow cylinder or a solid square.
2. **Inner FEA loop:** Point forces and moments are applied to the structure based on rotor and wing loads, such as rotor thrust, rotor torque and wing lift. The von-Mises stress ( $\sigma_{VM}$ ), the corresponding factor of safety and deflection of the various nodes are computed as

$$\sigma_{VM} = \left[ (\sigma_{11} - \sigma_{22})^2 + (\sigma_{22} - \sigma_{33})^2 + (\sigma_{33} - \sigma_{11})^2 + 6(\sigma_{23}^2 + \sigma_{12}^2 + \sigma_{13}^2) \right]^{1/2} \quad (28)$$

where  $\sigma_{ij}$  are components of the stress tensor and the factor-of-safety (FOS) is

$$\text{FOS} = \min(\sigma_{VM})_i \quad \forall i \in N \quad (29)$$

where  $N$  is the total number of beam elements.

3. **Update cross-section dimensions:** The mathematical constraints imposed for convergence are

$$|\text{FOS}_{\text{tar}} - \Delta\text{FOS}| \leq \min(\text{FOS}) \quad (30)$$

where  $\text{FOS}_{\text{tar}}$  is the target FOS, set to 1.5 and  $\Delta\text{FOS}$  is the allowable band, set to 0.1. A tolerance band for FOS is required as the “optimizer” is unlikely to converge to

an exact FOS, and for practical engineering purposes, a band will suffice. The maximum deflection is set to a fraction of the rotor radius (15%). The beam cross-section is increased (by 10%) if the factor of safety is too low or if the deflection is too high, and vice-versa, i.e., reduced by 10% if the deflection is below the threshold or if the FOS is higher than the target. Steps 2 and 3 are repeated till the FEA loop converges to the required factor of safety and deflection limits.

4. **Outer sizing loop:** The airframe weight is computed by multiplying the total volume of all the beam elements with the material density (assumed to be Aluminum,  $2,700 \text{ kg/m}^3$ ). This converged airframe weight from static finite element analysis replaces the fuselage weight from the AFDD empty weight formulae and the new GTOW, fuel required, power required are computed as part of the standard sizing loop in Fig. 3.

The use of FEA in sizing airframe structures also provides estimates of the natural frequencies and the mode-shapes. This information can be used in future stages of design to ensure sufficient separation between the airframe, blade natural frequencies and operating RPM range of the rotor(s).

## RESULTS AND DISCUSSION

### Sizing Mission

In previous work (Ref. 10), the use of unmanned multirotor VTOL platforms as autonomous logistics and resupply vehicles that can carry a human-sized payload at 60 mph was investigated. Such a mission is representative of low-altitude scouting, restock/resupply and autonomous evacuation of wounded personnel from disaster areas. The mission

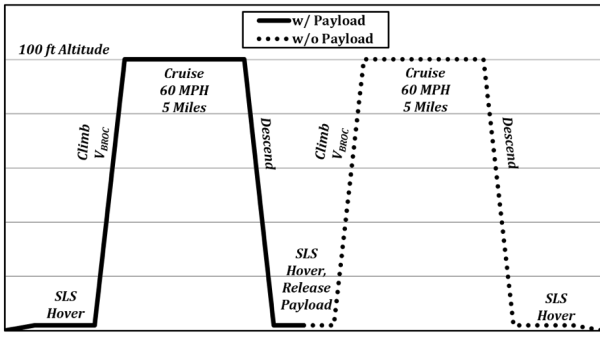


Fig. 7. Out-and-back resupply mission profile.

profile, shown in Fig. 7 is to deliver a 300 lb payload to a location 5 miles from the starting point and return to the point of origin. Payload release is modeled as a 5-minute hover segment, and return to base without the payload is assumed to occur at the same altitude and cruise speed as the outbound segment. Owing to the short-range mission chosen (for the scale of the vehicle considered), fuel weight does not constitute a large fraction of the total take-off weight. Therefore, variable-RPM designs are not considered. Though these designs have the potential to reduce rotor power requirements in cruise, the effect on sizing the entire vehicle is negligible for the mission chosen. Such a design may be more relevant for a longer-range mission.

### Convergence: Rotor Blade Weight Model

A representative example is used to study the convergence of the inner loop for sizing rotor blades, using the following operating parameters:

1. Rotor radius  $R = 1.0$  m
2. Rotor speed  $\Omega = 45.5$  rad/s
3. Blade thrust  $F_z = 463$  N
4. Blade torque  $Q_b = M_z = 130$  N-m
5. Blade chord  $c = 0.094$  m
6. Load factor  $n_z = 2.0$
7. Spar material is 0/90 carbon fiber
8. Skin material is 0/90 carbon fiber

The initial spar thickness  $t$  is set to 0.2% chord, and the initial skin thickness is set to zero. Using fixed-point iterations, the spar thickness  $t$  and skin thickness  $t_s$  are updated until both design parameters change by less than 1% across iterations. The convergence of the safety factor in the spar and skin are shown in Fig. 8. After an initial overshoot, both components operate well short of failure. The bending loads are amplified by the load factor  $n_z$ , through which the safety factor is incorporated.

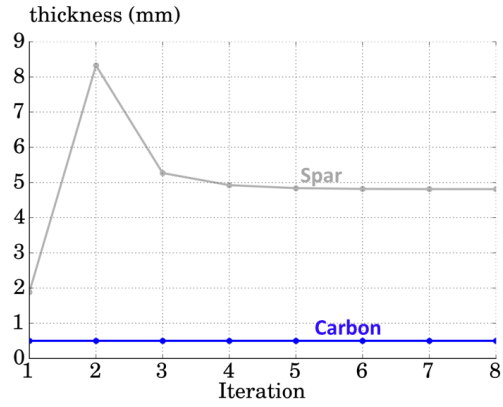


Fig. 9. Convergence of skin and spar thickness

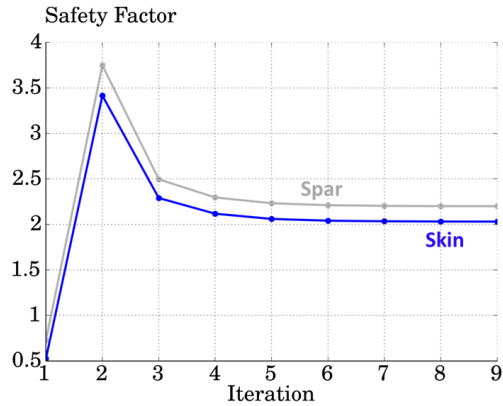
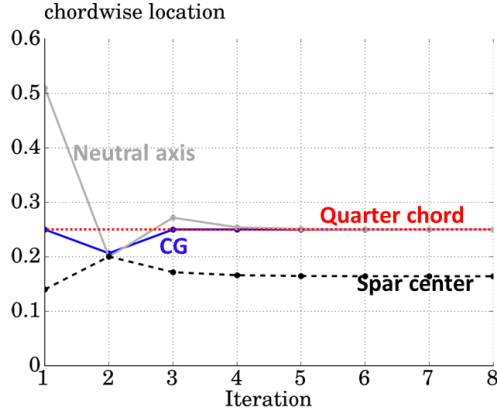


Fig. 8. Convergence of safety factors in spar and skin

The convergence of the independent parameters  $t/c$  and  $t_s/c$  is shown in Fig. 9. These parameters are directly adjusted by the iterative method until safety factors in each material are in the neighborhood of their prescribed values. If the thickness of any component reduces below 0.5 mm, it is rounded up to 0.5 mm, the thinnest possible layer that can be constructed. For the example chosen, the carbon fiber skin thickness converges immediately to the lower limit of 0.5 mm. The spar thickness, after some initial overshoots, converges to 4.8mm, i.e. the design corresponds to a nearly solid spar.

As part of the cross-section analysis, the location of the chordwise center of gravity location, neutral axis and spar location within the cross-section are computed and their convergence tracked and plotted in Fig. 10. As the spar is shifted forwards from  $0.25c$  to  $0.17c$ , the neutral axis correspondingly converges to quarter-chord. Leading-edge weights are also placed to shift the CG forwards to quarter-chord. These weights constitute less than 8% increase in blade weight.

Most of the axial stress in the spar and skin are caused by the flap bending moment due to blade lift instead of centrifugal force (the opposite of full-scale designs). The root bending moments must be borne by structural stiffness; the combination of centrifugal loads and blade elastic deflection is not sufficient to alleviate flap bending moment significantly. At



**Fig. 10. Convergence of CG, neutral axis and spar location**

smaller scales, rotor blade design criteria for stresses resemble those of aircraft wing design instead of those relevant to full-scale blades.

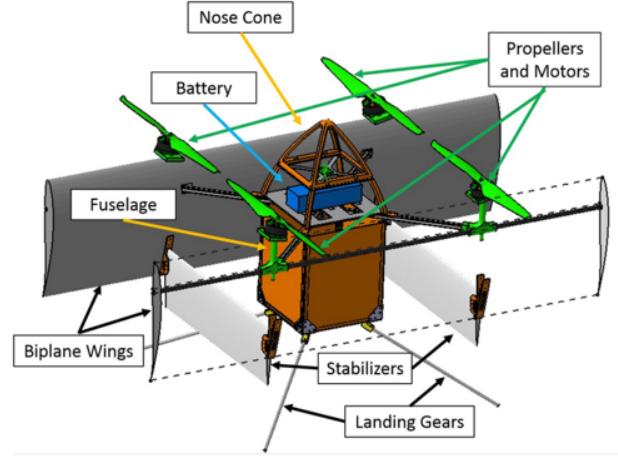
This convergence process is integrated into HYDRA’s sizing process in a manner to that used to integrate the physics-based airframe weight model, i.e. for every sizing iteration, the convergence process for rotor blade section properties is performed and the rotor group weight estimated from the physical dimensions of various members in the cross-section.

### Quad-Rotor Bi-Plane Tailsitter (QBT)

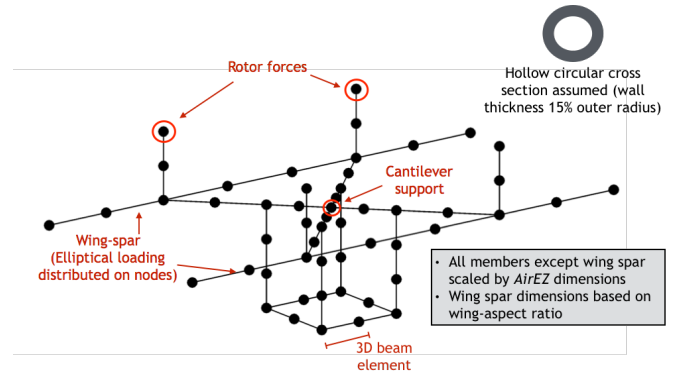
The Quad-Rotor Bi-plane Tailsitter (QBT) is a relatively new configuration that consists of four non-overlapping rotors and two wings in a bi-plane configuration. This tailsitter configuration was designed and developed at the University of Maryland (Ref. 11). One of the variants, known as “AirEZ”, was envisioned for package delivery (which takes place in the hover position). Cruise efficiency is achieved by transitioning to “airplane” mode by tilting the entire body of the vehicle.

Figure 11(a) shows a schematic of *AirEZ* in the hover configuration with the rotors, biplane wings, nose cone structure that houses the battery and avionics, fuselage for the payload and the landing gears. Figure 11(b) shows a skeletal structure, which closely mimics that of *AirEZ*, used in the present study for the layout of the airframe. The cross-section of *AirEZ* was based on commercially available Aluminum component with a complex cross-section, optimized for easy mechanical mating with other components. In the present study, the cross-section is assumed to be a hollow circle of wall thickness equal to 15% of the outer radius. Rotor forces and moments are applied as point loads on the beam nodes that support the rotor, and the wing-loads are applied at the nodes assuming an elliptical distribution loads on the spar that is housed in the wing; see Fig. 11(b). Only the loads at steady hover and cruise are considered for sizing the load-carrying members of the frame for *AirEZ*.

The lift generated by the wings is sub-divided into a series of point loads acting at beam nodes along the wing spar. Two wing lift distributions were investigated; a uniform distribution and an elliptical distribution. When integrated into



(a) “AirEZ” schematic



(b) FEA model

**Fig. 11. Quad-Rotor Bi-Plane model developed at University of Maryland and the FEA beam layout used in the present work.**

the vehicle sizing loop, the uniform lift distribution led to excessive airframe weights because high bending loads triggered the classical weight ballooning problem. This cascading problem was mitigated when an elliptical loading was assumed, which concentrates the load towards the center of spar and away from the tips. Such an assumption is also closer to the distribution of lift on a finite wing, where a decrease in tip load is observed because of the presence of wing-tip vortices. Figure 12 shows a schematic of the elliptic loading and the nodes on the wing-spar. The distributed lift per unit wing span is given by

$$L(x) = L_0 \sqrt{1 - \left(\frac{2x}{b}\right)^2}, \quad x \in [-b/2, b/2] \quad (31)$$

where  $b$  is the wingspan and  $L_0$  is  $4L_{\text{wing}}/\pi b$  and  $L_{\text{wing}}$  is the lift carried by each of the two wings, equal to half the vehicle weight in cruise. In the first instance, the increase in dynamic pressure over the wing because of the prop-rotor wash was not considered.

To demonstrate and test the workings of the FEA optimization, the QBT baseline configuration was subjected to

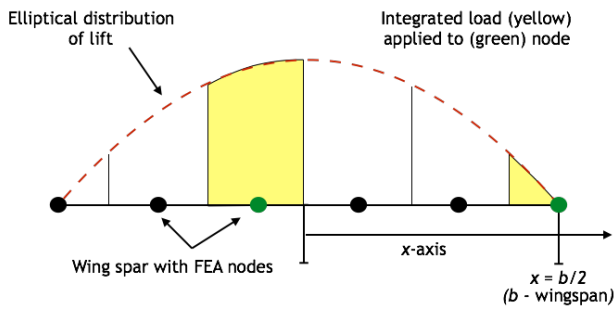
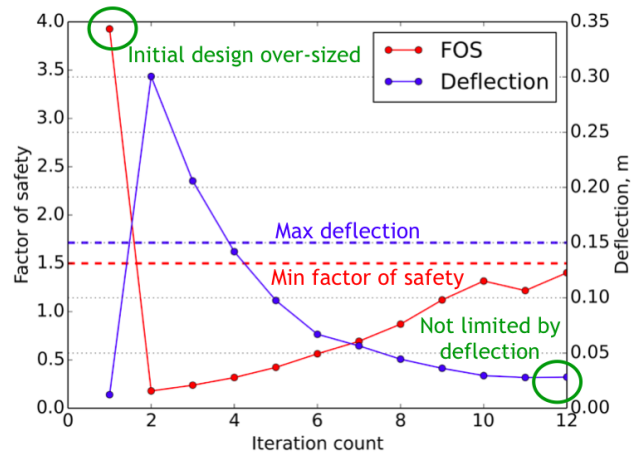


**Fig. 12. Schematic depicting the integration of the elliptic wing lift onto the FEA nodes as point loads.**

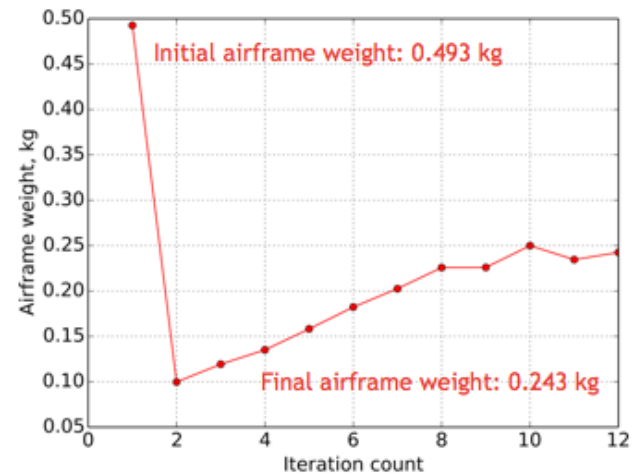
the loads experienced by the *AirEZ* configuration in hover and forward flight. The total weight of the vehicle was 3.6 kg, which was divided amongst the four rotors. The reaction torque at the support node was applied to the structure based on the direction of rotation of the rotors. In forward flight, a  $L/D$  ratio of the vehicle in cruise of 5 was obtained from experimental data (Ref. 11) and the net thrust produced by each rotor is equal to a quarter of the total vehicle drag. The weight of the vehicle was assumed to be carried entirely by the wings, with each wing carrying half the total lift (interference effects were neglected between the wings).

Figure 13(a) shows the variation of minimum FOS and maximum deflection amongst all beam elements against iteration count. The initial design had a minimum FOS of 3.92 and a maximum deflection of 0.02 m. The target FOS was set to  $1.5 \pm 0.1$  and the target maximum deflection was set to 0.15 m. Based on the thresholds set in the analysis, the original configuration appears to be over-designed. By changing the beam dimensions in accordance with the constraints placed on the system, the solution converged in 12 iterations. The final solution resulted in an overall minimum FOS of 1.4 and a maximum deflection of 0.028 m. In effect, the solution was driven the requirement on FOS rather than the deflection. Figure 13(b) shows the variation in airframe weight across iterations. The initial airframe configuration has a mass 0.493 kg, which was reduced to 0.243 kg at the end of the FEA-based optimization loop – 51% reduction in airframe weight. While it is difficult to mathematically guarantee a unique solution in terms of beam dimensions for arbitrary geometries, the optimization methodology was tested for different initial conditions, all of which resulted in the identical final configuration.

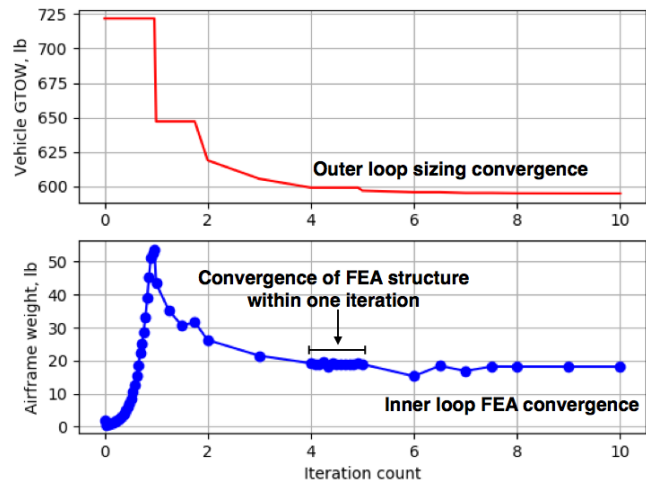
Figure 13(c) shows a representative convergence history of the outer sizing loop (shown in red) and the inner FEA loop (shown in blue). In this scenario, the empty weight of the airframe of the AFDD model is replaced with that obtained from FEA within each iteration. The solid circles in Fig. 13(c) represent the airframe weight for each FEA iteration. The number of FEA iterations required for convergence varies from one sizing iteration to the next, which is reflected in the dense or sparse presence of the blue solid circles. The ramp in the airframe weight history was attributed to an initial condition that is far from the final solution. Nonetheless, the methodology is robust and both inner and outer loops converge.



(a) Constraints



(b) Airframe weight



(c) Airframe weight

**Fig. 13. Convergence history of the FEA optimizer highlighting the: (a) Adherence to constraints, (b) Airframe weight, and (c) Inner and outer loop.**

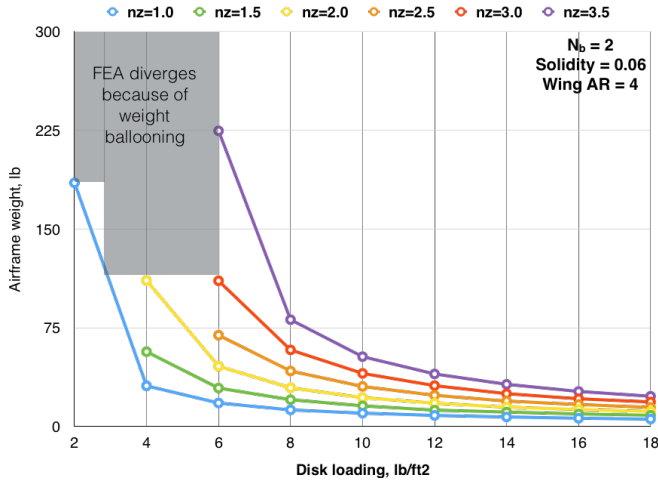


**Fig. 14. Sensitivity of FEA and QBT airframe design to rotor disk loading and load factor.**

In the AFDD82 model for the fuselage (see Eq. 27), the load factor  $n_z$  is part of the empirical fit. In the FEA analysis, the rotor thrust and wing lift are multiplied by the load factor, consequently requiring the structure to maintain the factor of safety and deflection limits at the design load levels. In this study, the number of blades was set to 2, rotor solidity set to 0.06 and the wing aspect ratio prescribed as 4.0.

Figure 14 shows the variation of airframe weight with disk loading for different design load factors. At a constant load factor, the airframe weight increases as the disk loading is decreased. This result can be understood as follows: the rotor radius increases as disk loading decreases and consequently, the airframe, which is a scaled model of the *AirEZ* airframe based on rotor radius also increases in dimensions. This increase in the length of the beam increases the airframe weight. At very low disk loadings, this increased airframe weight increases the total vehicle weight, which increases the loads on the vehicle and cascades into the classical weight ballooning problem, resulting in divergent iterations. It should be noted that the AFDD82 model for the fuselage results in a convergent design. One interpretation of this convergence is that legacy weight models may contain inaccuracies and fail to model certain physical phenomena when applied to new configurations for which they have not been tuned.

In general, as the load factor is increased the airframe weight increases for a given disk loading, as shown in Fig. 14. The weight ballooning problem persists irrespective of the load factor, which results in an infeasible design space in the upper left corner of Fig. 14. However, at higher disk loadings, the rotor radius is small and, consequently so are the airframe dimensions. This trend linking disk loading to airframe weights persists at the various load factors considered.

Figure 15 shows the position of the beam elements under hover and forward flight loading conditions obtained at the end of a design cycle. It was noted that the limiting flight condition was forward flight because of the loading on the wings and the solution was stress limited rather than deflection lim-

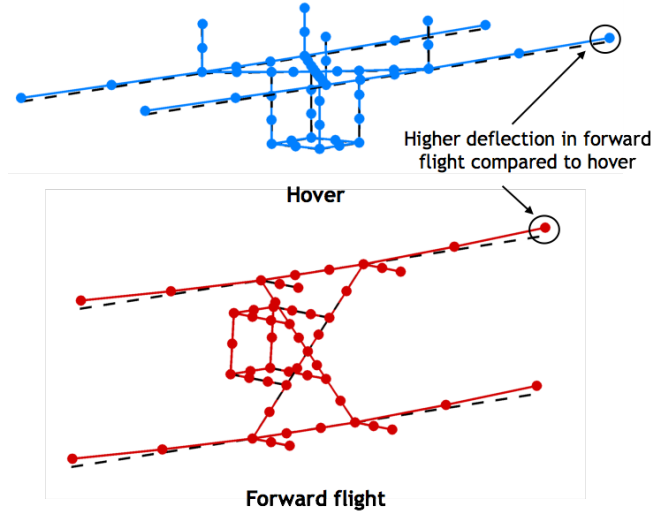


**Fig. 15. Representative deflections of the beam elements in hover and forward flight.**

ited. In both conditions, the nodes where the rotor loads are applied showed a maximum deflection of only 1.1% of the rotor radius. The minimum factor of safety in hover mode for the von-Mises stress was 1.56 and 1.42 in forward flight mode. The requirement was for the minimum FOS to lie in 0.1 band around 1.5. Therefore, it is evident that the limiting loading condition is forward flight for the QBT configuration.

### Design Space and Practical Limits

Table 1 shows the range of the various design parameters explored in this study, which is typical of the ranges present in various design studies. The cruise wing lift fraction was set to 1.0, implying that the rotors produce thrust to overcome the drag of the vehicle and the weight of the vehicle is entirely carried by the wing. The load factor was set to 3.5, which is reflected the thrust of the rotors and lift on the wings. A factorial search of the design space results in a total of 2,160 possible design combinations.

**Table 1. Design parameters and their ranges.**

| Rotor parameter             | Range       | Units    |
|-----------------------------|-------------|----------|
| Disk Loading, $DL$          | 1 – 18      | lb/sq.ft |
| Rotor Solidity, $\sigma$    | 0.06 – 0.14 |          |
| Number of blades, $N_b$     | 2, 3, 4     |          |
| Hover tip speed, $V_{TIP}$  | 80 – 150    | m/s      |
| Wing parameter              | Range       | Units    |
| Aspect ratio, $AR$          | 4 – 10      |          |
| Cruise lift fraction, $f_w$ | 1.0         |          |

The rotor power calculations in the modified disk model do not take into account local effects like airfoil static stall and advancing blade stresses. Therefore, depending on the choice

**Table 2. Comparison of best design for minimum fuel and minimum GTOW with and without physics-based weight model for airframe and rotor blades.**

| Rotor parameter                  | AFDD Model (Empirical) |               | Airframe FEA   |               | Airframe FEA + Rotor Analysis |               |
|----------------------------------|------------------------|---------------|----------------|---------------|-------------------------------|---------------|
|                                  | 1<br>Min Power         | 2<br>Min GTOW | 3<br>Min Power | 4<br>Min GTOW | 5<br>Min Power                | 6<br>Min GTOW |
| Number of blades, $N_b$          | 4                      | 4             | 4              | 4             | 4                             | 4             |
| Disk Loading $DL$ , lb/sq.ft     | 1.0                    | 12.0          | 1.0            | 2.0           | 1.0                           | 2.0           |
| Solidity, $\sigma$               | 0.06                   | 0.14          | 0.06           | 0.06          | 0.06                          | 0.06          |
| Flap frequency, $\nu_\beta$ /rev | 1.05                   | 1.05          | 1.05           | 1.05          | -                             | -             |
| Hover $C_T/\sigma$               | 0.101                  | 0.149         | 0.101          | 0.115         | 0.101                         | 0.090         |
| Gross Weight, lbs                | 729                    | 596           | 887            | 747           | 775                           | 719           |
| Empty Weight, lbs                | 422                    | 287           | 578            | 439           | 467                           | 409           |
| Airframe Weight, lbs             | 88                     | 32            | 181            | 132           | 138                           | 121           |
| Rotor Weight, lbs                | 36                     | 5             | 53             | 20            | 22                            | 9             |
| Installed Power, hp              | 29.5                   | 74.9          | 35.8           | 40.5          | 31.1                          | 42.3          |
| Radius, ft                       | 5.90                   | 1.41          | 6.91           | 4.26          | 6.22                          | 4.11          |
| Tip speed, ft/s                  | 80.0                   | 150.0         | 80.0           | 100.0         | 80.0                          | 120.0         |

| Rotor parameter   | 1<br>Min Power | 2<br>Min GTOW | 3<br>Min Power | 4<br>Min GTOW | 5<br>Min Power | 6<br>Min GTOW |
|-------------------|----------------|---------------|----------------|---------------|----------------|---------------|
| Aspect ratio $AR$ | 4.0            | 4.0           | 4.0            | 4.0           | 4.0            | 4.0           |
| Span, ft          | 16.3           | 13.5          | 19.1           | 16.6          | 17.2           | 16.1          |

of input variables (rotor solidity, tip speed and disk loading) the simplified performance calculations will fail to identify designs which are not practical. When the hover blade loading coefficient  $C_T/\sigma$  is above 0.13, the mean operating lift coefficient of the rotor sections is 0.78. Depending on the twist and chord distribution of the rotor sections, certain sections may operate close to stall, leaving little margin for maneuvers or gust tolerance. Therefore, designs that exceed this threshold are discarded. This vehicle operates in axial flight during all mission phases (except transition between hover and cruise). For these flight conditions, momentum

Because the rotors operate in either hover or axial flight (forward flight in airplane mode), the prediction in power obtained using the simpler momentum theory was well aligned with the use of higher fidelity free-vortex methods. Interference effects between the rotor and wing in the free-vortex model was considered beyond the scope of the present work, and will be implemented in the future. Therefore, the present work include the momentum theory predictions in all the results.

### Comparison of Empirical and Physics-Based Model

A factorial search was performed on the design space to evaluate the differences in the “optimal” design between the use of the AFDD empirical fits and the use of the physics-based model (for only the airframe). For the purposes of this study,

the optimal design was chosen based on the requirement for minimum installed power or minimum gross take-off weight (GTOW). The vehicle sized was the QBT in accordance with the mission profile shown in Fig. 7. It should be noted that the transition phases from hover to forward flight and vice-versa were not considered in the study. In all cases, a battery-based propulsion system was chosen and the results are presented in Table 2. Shown on the first column are key design parameters of the QBT. Key inferences are as follows

1. Depending on a combination of safety factor, spar material and skin material chosen, the weight of the rotor blades may vary by as much as 100%. For example, using a Titanium spar instead of 0/90 carbon fiber results in almost doubling of blade weights. In the statistical model, this variation between materials may be incorporated as a “technology factor” that reduces blade weights by 50%.
2. In many cases, the flap frequency  $\nu_\beta$  is in excess of 3/rev for these small-scale blades. There is no reliable data for the AFDD weight model in this region of the design space. Despite these restrictions, if the AFDD model is used to predict the weight, the resulting blade mass may increase from 5 kg to 45 kg – the variation introduced by the flap frequency parameter introduces a lot of uncertainty and must be interpreted carefully; using a physics-based model to predict blade weight avoids this

confusion entirely.

3. The best design for minimum power with the AFDD model resulted in a vehicle with a disk loading (DL) of  $1 \text{ lb/ft}^2$ , which is extremely low (a Robinson R-22 is  $2.2 \text{ lb/ft}^2$ ). As the hover power is higher compared to power requirements in forward flight, a low DL is beneficial in minimizing induced losses. However, this results in a large radius of 6.89 ft, which consequently results in a vehicle with a large footprint. No constraints were placed on the overall dimension of the vehicle.
4. The designs for minimum GTOW occur at higher DLs because of a decrease in rotor radius, which decreases the airframe dimensions and consequently the overall weight of the vehicle. With the AFDD model, the GTOW drops by 135 lb compared to the solution for minimum power. The trend is reflected in the airframe weight which reduced from 88 lb to 32 lb.
5. It is interesting to note that the weights are quite similar between the two optimal cases with the FEA model in the sizing loop. This result when compared to the spread in GTOW using the AFDD model can be attributed to the ability of the physics based model to weed out non-physical designs from first-principles. The least vehicle weight for the QBT was 719 lb with an empty weight fraction of 56.8%.

## CONCLUSIONS

In this paper, a physics-based model for sizing rotor blades and airframe structures for an unconventional VTOL configuration has been presented. The physics-based models are iteratively used to size each component in inner loops within the sizing convergence loop. For successful designs each of these models converge in 8 – 12 sub-iterations. The modified sizing method was applied for sizing a quad-rotor bi-plane tail sitter (QBT) configuration for a resupply mission with a 5 mile radius of action with a 300-lb payload. The specific conclusions of the study are

1. For sub-scale and intermediate-scale vehicles ( $\text{GTOW} \leq 1,000 \text{ lbs}$ ) with multiple rotors, the blades contribute a very small fraction of the gross weight to total vehicle weight. For the mission chosen, less than 2% of the vehicle weight is allocated for the rotor group, which does not drive the sizing as dominantly as in the case of full-scale vehicles. In full-scale designs, the blade weight is closer to 6% of the gross take-off weight, where it can influence other empty group weights and alter the final design noticeably.
2. For sub-scale designs, the best designs for performance require low tip speeds and lightweight blades. Owing to low centrifugal loads, the use of tip weights to reduce rotor flap bending moment results in a blade that is 10 times heavier, and is not an efficient option.

3. The “inner loop” in the airframe FEA ensures that all members are sized according to their individual operating limits, thus maximizing structural effectiveness for the expected loading conditions. The FEA-based weight model also accounts for an increase in weight with increase in expected load, i.e., the classical weight ballooning problem. At higher load factors and lower disk loadings, the sizing iterations do not converge for the QBT configuration.
4. The powerplant capacity is driven entirely by hover power requirements. Low disk loading designs, though less compact and heavier than high-disk loading configurations, require less installed power because the available rotor disk area is larger and induced power requirements are lower.
5. Design for minimum gross weight results in a higher rotor disk loading and higher tip speed compared to design for minimum installed power. For the compact vehicles (minimum weight), the use of a modified AFDD weight model results in 30% difference in gross take-off weight compared to a physics-based design using the actual layout of the structure. For the minimum power design (larger vehicle), the difference in predictions obtained with the two models is small (2%). It may be better to use the physics-based model throughout the design process, given the potential differences between the statistical weight model and the loads-based method.

## ACKNOWLEDGEMENTS

This work was supported by the U.S. Army Research Laboratories under UMD-CRA with Rajenesh Singh as the technical monitor. The authors would like to acknowledge Brent Mills for providing data on the propulsion systems, Vikram Hrishikeshavan and VT Nagaraj for technical discussion on rotorcraft design.

## REFERENCES

- <sup>1</sup>Johnson, W., “NDARC - NASA Design and Analysis of Rotorcraft Validation and Demonstration,” American Helicopter Society Aeromechanics Specialists Meeting, San Francisco, CA, January 2008.
- <sup>2</sup>Avera, M., Kang, H., and Singh, R., “Comprehensive Rotorcraft Analysis for Preliminary Design and Optimization,” Proceedings of the 71st Annual Forum of the American Helicopter Society, Virginia Beach, VA, May 5–7, 2015.
- <sup>3</sup>Sridharan, A., Govindarajan, B. M., Nagaraj, V. T., and Chopra, I., “Design Considerations of a Lift-Offset Single Main Rotor Compound Helicopter,” American Helicopter Society Specialists Meeting on Aeromechanics Design for Vertical Lift, San Francisco, CA, January 20–22, 2016.
- <sup>4</sup>Ardema, M., Chambers, M., Patron, A., Hahn, A., Hirokazu, M., and Moore, M., “Analytical Fuselage and Wing

Weight Estimation of Transport Aircraft: NASA Technical Memorandum 110392,” , April 1996.

<sup>5</sup>Tishchenko, M. N. and Nagaraj, V. T., “ENAE634 Helicopter Design Lecture Notes,” , 2010.

<sup>6</sup>Sridharan, A., Govindarajan, B. M., Nagaraj, V. T., and Chopra, I., “Towards Coupling of Comprehensive Analysis into Design Sizing of a High-Speed Asymmetric Compound Helicopter,” 42<sup>nd</sup> European Rotorcraft Forum, Lille, France, September 5–7, 2016.

<sup>7</sup>Rubenstein, G., Moy, D. M., Sridharan, A., and Chopra, I., “A Python-based Framework for Real-time Simulation Using Comprehensive Analysis,” 72<sup>nd</sup> Annual Forum of the American Helicopter Society, West Palm Beach, FL, May 16–18, 2016.

<sup>8</sup>Govindarajan, B. M. and Leishman, J. G., “Predictions of Rotor and Rotor/Airframe Configurational Effects on Brownout Dust Clouds,” *Journal of Aircraft*, Aug 2015, pp. 1–16.

<sup>9</sup>Moodie, A. and Yeo, H., “Design of a Cruise-Efficient Compound Helicopter,” Vol. 57, (3), 2012.

<sup>10</sup>“Unmanned Resupply Vehicle Could Reduce Combat Casualties,” <https://www.army.mil/article/174907/>.

<sup>11</sup>Phillips, B. and Hrishikeshavan, V. and Chopra, I. and Rand, O., “Design and Development of a Scaled Quadrotor Biplane with Variable Pitch Proprotors for Rapid Payload Delivery,” Proceedings of the 72<sup>nd</sup> Annual Forum of the American Helicopter Society, West Palm Beach, FL, May 16–18, 2016.